# Mechanism of Photogenerated Reactive Oxygen Species and Correlation with the Antibacterial Properties of Engineered Metal-Oxide Nanoparticles

Yang Li,[†,‡,§] Wen Zhang,[‡,§] Junfeng Niu,[†] and Yongsheng Chen[‡,*]

[†]State Key Laboratory of Water Environment Simulation, School of Environment, Beijing Normal University, Beijing 100875, People's Republic of China and [‡]School of Civil and Environmental Engineering, Georgia Institute of Technology, Atlanta, Georgia 30332, United States. [§]The first and second authors contributed equally to this work.
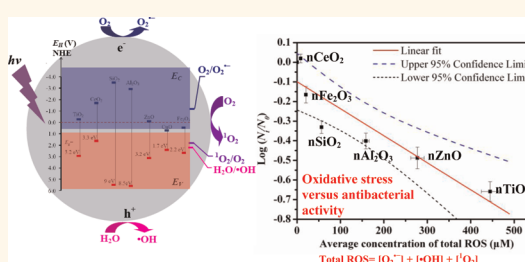
Despite concerns about the potential environmental and ecological risks posed by the many applications of engineered nanoparticles (NPs),[1−3] such particles are a promising antibacterial agent owing to their photoactive bactericidal effects.[4,5] Several metal-oxide NPs, such as $TiO_2$ nanoparicles ($nTiO_2$), have been reported to possess significant antibacterial activity, and these have been extensively studied.[5−7] Other metal-oxide NPs, including nCuO, $nSiO_2$, and nZnO, also exhibit excellent antibacterial activity against both Gram-positive and Gram-negative bacteria.[8−12]

Oxidative stress induced by reactive oxygen species (ROS) generation in NP systems is thought to be the main mechanism of their antibacterial activity.[2,13,14] In particular, many previous studies have explored the photogeneration of ROS on the surfaces of metal-oxide NPs.[5,15] The general principle is that when illuminated by light with photoenergy greater than the band gap, the electrons ($e^−$) of NPs are promoted across the band gap to the conduction band, which creates a hole ($h^+$) in the valence band.[5] Electrons in the conduction band and holes in the valence band exhibit high reducing and oxidizing power, respectively.[15] The electron can react with molecular oxygen to produce superoxide anion ($O_2^{•−}$) through a reductive process.[15] The hole can abstract electrons from water and/or hydroxyl ions to generate hydroxyl radicals ($^•OH$) through an oxidative process.[15] Singlet oxygen ($^1O_2$) is mostly produced indirectly from aqueous reactions of $O_2^{•−}$.[5] $^•OH$ is a strong and nonselective oxidant[5] that can damage virtually all types of organic biomolecules, including carbohydrates, nucleic acids, lipids, proteins, DNA,

and amino acids.[16] $^1O_2$ is the main mediator of photocytoxicity and can irreversibly damage the treated tissues,[17] causing biomembrane oxidation and degradation.[18] Although $O_2^{•−}$ is not a strong oxidant, as a precursor for $^•OH$ and $^1O_2$, $O_2^{•−}$ also has significant biological implications.[19] Consequently, these three types of ROS ($O_2^{•−}$, $^•OH$, and $^1O_2$)

**ABSTRACT**



Oxidative stress induced by reactive oxygen species (ROS) is one of the most important antibacterial mechanisms of engineered nanoparticles (NPs). To elucidate the ROS generation mechanisms, we investigated the ROS production kinetics of seven selected metal-oxide NPs and their bulk counterparts under UV irradiation (365 nm). The results show that different metal oxides had distinct photogenerated ROS kinetics. Particularly, $TiO_2$ nanoparticles and ZnO nanoparticles generated three types of ROS (superoxide radical, hydroxyl radical, and singlet oxygen), whereas other metal oxides generated only one or two types or did not generate any type of ROS. Moreover, NPs yielded more ROS than their bulk counterparts likely due to larger surface areas of NPs providing more absorption sites for UV irradiation. The ROS generation mechanism was elucidated by comparing the electronic structures (*i.e.*, band edge energy levels) of the metal oxides with the redox potentials of various ROS generation, which correctly interpreted the ROS generation of most metal oxides. To develop a quantitative relationship between oxidative stress and antibacterial activity of NPs, we examined the viability of *E. coli* cells in aqueous suspensions of NPs under UV irradiation, and a linear correlation was found between the average concentration of total ROS and the bacterial survival rates ($R^2 = 0.84$). Although some NPs (*i.e.*, ZnO and CuO nanoparticles) released toxic ions that partially contributed to their antibacterial activity, this correlation quantitatively linked ROS production capability of NPs to their antibacterial activity as well as shed light on the applications of metal-oxide NPs as potential antibacterial agents.

**KEYWORDS:** antibacterial activity · nanoparticles · reactive oxygen species · ion release · UV irradiation

contribute to the major oxidative stress in biological systems. Although many previous studies have explored ROS generation by various metal-oxide NPs, to the best of our knowledge, little research has examined the role of the electronic properties (e.g., band energy edge structures) of metal-oxide NPs in ROS generation.[14] A deeper understanding in this aspect would allow us to interpret the underlying ROS generation mechanisms, potentially predict the amount of ROS generation or the antibacterial activity of newly synthesized metal-oxide NPs, and effectively reduce experimental testing costs.

A comprehensive literature review on ROS generation by NPs is summarized in Table S1 of the Supporting Information (SI). Although a consensus on the ROS production of different NPs was difficult to reach among various studies, almost all engineered NPs appear to produce ROS under certain circumstances. Unfortunately, differences in the sources or synthetic methods of NPs, experimental conditions (e.g., with or without light illumination, particle size and concentration), and solution chemistry (e.g., pH and ionic strength) largely hamper quantitative comparisons among different studies on ROS production for the same NPs. For example, some studies detected ROS in $nTiO_2$ suspensions under dark conditions,[20,21] whereas other studies did not.[2] Furthermore, in one study $nTiO_2$ in microbial growth medium induced the generation of $O_2^{\bullet-}$,[5] but in another study under similar biotic conditions it did not.[2] Previous studies reported that $nCeO_2$ suppressed ROS production and protected cells against oxidant injury.[13,22] Conversely, $nCeO_2$ inhibited Escherichia coli (E. coli) owing to oxidative stress.[23] Therefore, to compare the antibacterial activity of different NPs, distinguishing and quantifying each type of ROS produced under the same experimental conditions is essential.

Although ROS production by NPs is closely related to their antibacterial activity, quantitative relationships between the ROS production and antibacterial activity of NPs have not been well established.[7,24] One successful example is that the mortality rate of E. coli cells was linearly correlated with the concentration of $^{\bullet}OH$ generated from $nTiO_2$.[7] Furthermore, the antibacterial activity of nZnO suspension was linearly proportional to the concentration of $H_2O_2$ (a derivative of $O_2^{\bullet-}$).[24] However, not all ROS (i.e., $^1O_2$ and $O_2^{\bullet-}$) were taken into account when correlating the antibacterial activity of NPs. Considering the thousands of new NPs that will be utilized in the near future, it is impossible for every type of NP to go through antibacterial experiments, which is costly and labor-intensive. Thus, the development of quantitative relationships between the ROS production and antibacterial activity of NPs for rapid toxicological screening to rank NPs for priority in vivo testing is crucial.

In this study, we selected seven types of metal-oxide NPs ($nTiO_2$, $nCeO_2$, $nZnO$, $nCuO$, $nSiO_2$, $nAl_2O_3$, and

$nFe_2O_3$) as case studies because of their broad application in industrial products and their antibacterial properties.[8,10,25−28] On these NPs we investigated the generation of three types of ROS ($^1O_2$, $^{\bullet}OH$, and $O_2^{\bullet-}$) under UV irradiation (365 nm). The ROS generation mechanism was analyzed by comparing the band energy structures of the metal oxides with the redox potentials ($E_H$) of different ROS. To elucidate the effect of primary particle size on ROS generation, the bulk counterparts of these NPs ($bTiO_2$, $bCeO_2$, $bZnO$, $bCuO$, $bSiO_2$, and $bFe_2O_3$) were also quantified. Furthermore, we systematically studied the antibacterial activity of the NPs on E. coli cells as the model bacterium, which was then correlated with the average concentration of total ROS of different NPs as an indicator of oxidative power. Overall, this work is aimed at developing a theoretical framework for predicting the oxidative stress of metal-oxide NPs and providing insight into the application potential of engineered NPs as antibacterial agents.

## RESULTS AND DISCUSSION

**Generation Kinetics of $O_2^{\bullet-}$, $^{\bullet}OH$, and $^1O_2$.** Figure 1 shows the changes in the absorption spectrum of the particle suspension after 48 h UV irradiation. The absorption peak at $\lambda = 470$ nm indicates the production of $O_2^{\bullet-}$. Clearly, $nTiO_2$, $nZnO$, $nCeO_2$, $nFe_2O_3$, and $bZnO$ generated $O_2^{\bullet-}$ under UV irradiation, whereas none of the other three types of NPs and their bulk counterparts produce measurable amount of $O_2^{\bullet-}$ (Figure S3). In the absence of particles or in dark conditions, no absorption peaks were detected for all particle suspensions.

Figure 2a,b present the $^{\bullet}OH$ formation kinetics of different metal-oxide NPs and their bulk counterparts under UV irradiation. A control test performed in the absence of metal oxides demonstrated that the concentration of p-chlorobenzoic acid (pCBA) decreased by only $3.2 \pm 0.2\%$ after 48 h UV irradiation, which indicates that the photolysis of pCBA was negligible. Figure 2a shows that $nTiO_2$ had the highest $^{\bullet}OH$ generation rate, followed by nZnO and $nFe_2O_3$. For bulk materials, only bZnO and $bTiO_2$ produced noticeable $^{\bullet}OH$. The generation rate for bZnO was much faster than that for $bTiO_2$ within 8 h UV irradiation; however, $^{\bullet}OH$ generation by bZnO appeared to cease after approximately 8 h (Figure 2b). The other NPs and their bulk counterparts did not produce significant pCBA degradation under UV irradiation (data not shown), which indicates that no measurable amount of $^{\bullet}OH$ was produced. In the dark, none of these metal oxides produced detectable $^{\bullet}OH$ within the experimental period (48 h).

Figure 2c shows that $^1O_2$ generation was observed only in $nTiO_2$, $nSiO_2$, $nAl_2O_3$, and nZnO suspensions; other types of NPs and all seven types of bulk materials did not induce significant degradation of furfuryl alcohol (FFA) (data not shown). Again, $nTiO_2$ had the
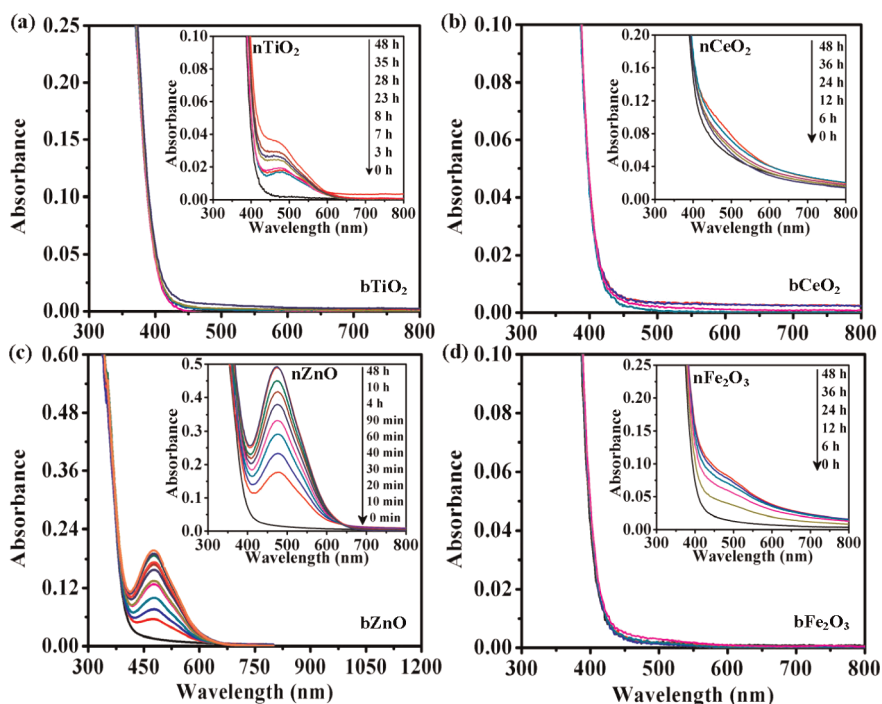
**Figure 1.** $O_2^{\bullet-}$ generation kinetics of various NPs and their bulk counterparts under UV irradiation as indicated by the reduction of 100 $\mu$M XTT (intensity of 0.78 mW/cm$^2$, room temperature of 22.5 °C, initial pH of 5.6, and initial particle concentration of 5.0 mg/L).

highest $^1O_2$ generation rate, followed by nAl$_2$O$_3$, nZnO, and nSiO$_2$. In the absence of NPs or bulk materials, approximately 4.1 $\pm$ 0.3% FFA was degraded, which indicates the photolysis of FFA under UV irradiation was negligible. In the dark, no $^1O_2$ was detected for any of these metal oxides within the experimental period (data not shown).

**ROS Concentration Generated by Various NPs and Their Bulk Counterparts.** Table 1 summarizes the average molar concentrations of the three types of ROS ($^{\bullet}$OH, $^1O_2$, and $O_2^{\bullet-}$) for different metal oxides, which were computed using eq 1. Bulk particles other than bTiO$_2$ and bZnO did not produce measurable ROS, whereas NPs other than nCuO generated ROS. At the same mass concentrations and UV irradiation, NPs generated more ROS than their bulk counterparts. The average concentration of total ROS (the sum of the concentrations of three types of ROS) followed the order nTiO$_2$ > nZnO > nAl$_2$O$_3$> nSiO$_2$ > nFe$_2$O$_3$ > nCeO$_2$ > nCuO and bZnO > bTiO$_2$. It was observed that (1) among NPs, nZnO generated the most $O_2^{\bullet-}$, followed by nFe$_2$O$_3$, nTiO$_2$, and nCeO$_2$, whereas for bulk materials, only bZnO favors $O_2^{\bullet-}$ generation; (2) nTiO$_2$ generated the most $^{\bullet}$OH, which was approximately 2-fold and 6-fold more than that generated by nZnO and nFe$_2$O$_3$. For bulk materials, bTiO$_2$ generated approximately 2.5-fold more $^{\bullet}$OH than bZnO did. (3) nTiO$_2$ generated the most $^1O_2$, followed by nAl$_2$O$_3$, nZnO, and nSiO$_2$. The enhanced ROS generation power of NPs compared to their bulk counterpart is likely due to their larger surface areas, which provide more available reaction

sites for UV absorption.[1,29] Other potentially size-dependent properties (e.g., light absorption or scattering, defect sites, and structural disorder) may also lead to the difference in photoactivity.[30]

**Electronic Structures of Metal Oxides and Their Relationship to ROS Generation.** Production of a specific type of ROS (e.g., $^{\bullet}$OH, $^1O_2$, or $O_2^{\bullet-}$) on metal oxides under UV illumination could be related to the electronic structures of the metal oxides as well as the redox potentials ($E_H$) of the different ROS generation reactions.[31,32] The electronic structure of metal-oxide NPs is characterized by the band gap ($E_g$), which is essentially the energy interval between the valence band ($E_v$) and the conduction band ($E_c$), each of which has a high density of states. Table S4 lists the literature values of $E_g$, $E_c$, and $E_v$ for the seven types of pristine metal oxides. From the interfacial energy perspective, ROS generation is dictated by the interfacial electron transfer process, which is driven by photoexcitation in this case. Only the metal-oxide NPs with $E_g$ less than the incident photon energy (i.e., approximately 5.45 $\times$ 10$^{-19}$ J or 3.4 eV for the 365 nm UV) can be photoexcited. Under UV excitation, electrons are promoted from the valence band to the conduction band, with the concomitant generation of a hole in the valence band. The photoexcited electrons and holes then react with an aqueous electron acceptor (i.e., molecular oxygen) and donor (i.e., water and hydroxyl ions), respectively, to produce different types of ROS.

In aqueous environments, the band edge energies shift to higher or lower energy levels owing to the
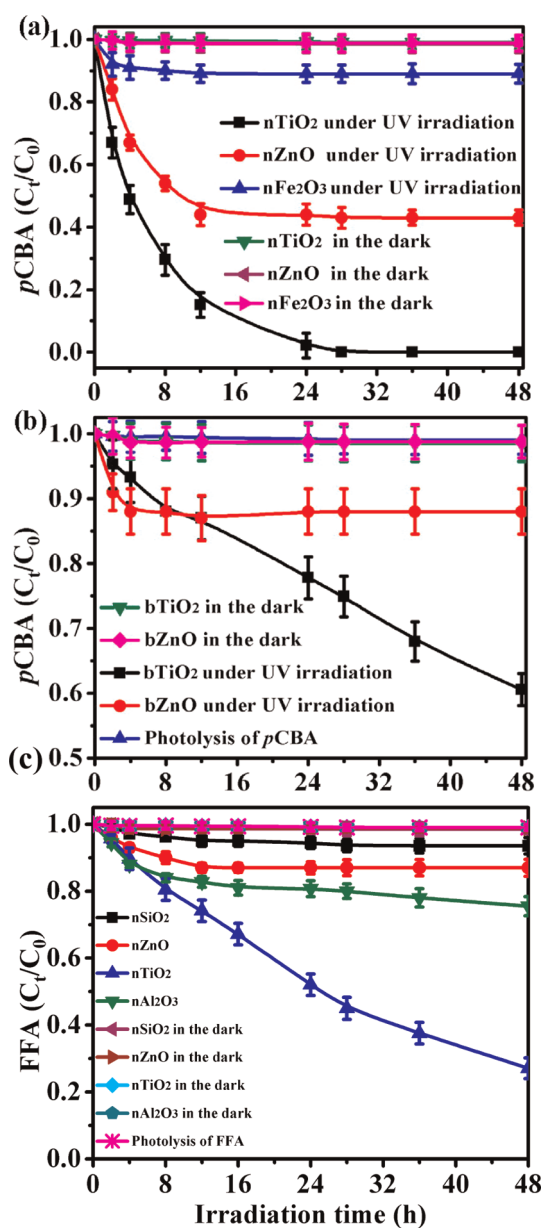
## (a)



Legend:
- nTiO₂ under UV irradiation
- nZnO under UV irradiation
- nFe₂O₃ under UV irradiation
- nTiO₂ in the dark
- nZnO in the dark
- nFe₂O₃ in the dark

## (b)



Legend:
- bTiO₂ in the dark
- bZnO in the dark
- bTiO₂ under UV irradiation
- bZnO under UV irradiation
- Photolysis of $p$CBA

## (c)



Legend:
- nSiO₂
- nZnO
- nTiO₂
- nAl₂O₃
- nSiO₂ in the dark
- nZnO in the dark
- nTiO₂ in the dark
- nAl₂O₃ in the dark
- Photolysis of FFA

**Figure 2.** •OH generation kinetics indicated by the degradation of 20 $\mu$M $p$CBA (a, b) and $^1O_2$ generation kinetics indicated by the degradation of 0.85 mM FFA (c) by various NPs and their bulk counterparts under UV irradiation (other conditions were the same as in Figure 1).

formation of the space charge layer as well as the electrostatic double layer (or Helmholtz layer) within the interface between the metal oxides and aqueous solution.[31,33] The relevant $E_c$ and $E_v$ band edge energies at a pH of 5.6 (the initial suspension pH during photochemical experiments) were calculated by the Nerstian relation:[34]

$$E_{c, pH} = E_c + 0.059 \times (PZZP - pH) \quad (1)$$

$$E_{v, pH} = E_v + 0.059 \times (PZZP - pH) \quad (2)$$

where PZZP is the point of zero zeta potential of the semiconductor materials, which are available in the

**TABLE 1. Average Concentrations of ROS Generated by Different Metal Oxides under UV Irradiation**

| particles | | •OH ($\mu$M) | $^1O_2$ ($\mu$M) | $O_2^{\bullet-}$ ($\mu$M) | total ($\mu$M) |
|---|---|---|---|---|---|
| TiO₂ | NPs | 19.3 ± 0.8 | 417.3 ± 18.8 | 8.0 ± 0.4 | 442.9 ± 20.0 |
| | bulk | 4.9 ± 0.2 | N.D.$a$ | N.D. | 4.9 ± 0.2 |
| CeO₂ | NPs | N.D. | N.D. | 8.4 ± 0.2 | 8.4 ± 0.2 |
| | bulk | N.D. | N.D. | N.D. | 0 |
| SiO₂ | NPs | N.D. | 56.5 ± 2.5 | N.D. | 56.5 ± 2.5 |
| | bulk | N.D. | N.D. | N.D. | 0 |
| Al₂O₃ | NPs | N.D. | 158.5 ± 8.0 | N.D. | 158.5 ± 8.0 |
| | bulk | N.D. | N.D. | N.D. | 0 |
| ZnO | NPs | 9.5 ± 0.6 | 100.8 ± 6.4 | 167 ± 8.6 | 277.3 ± 15.6 |
| | bulk | 1.9 ± 0.1 | N.D. | 81.8 ± 0.3 | 83.7 ± 0.4 |
| CuO | NPs | N.D. | N.D. | N.D. | 0 |
| | bulk | N.D. | N.D. | N.D. | 0 |
| Fe₂O₃ | NPs | 2.3 ± 0.1 | N.D. | 18.1 ± 1.1 | 20.4 ± 1.2 |
| | bulk | N.D. | N.D. | N.D. | 0 |

$^a$ N.D. indicates that ROS were not detected or were not statistically significant.
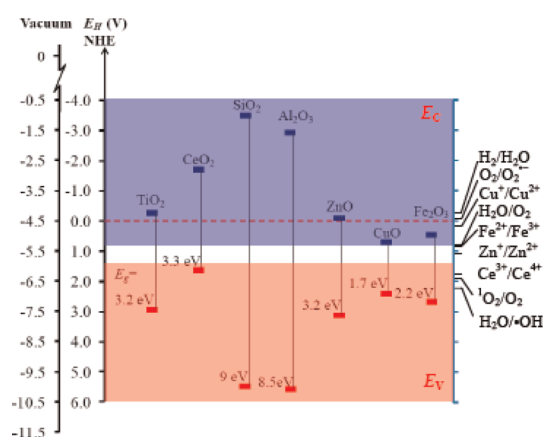


**Figure 3.** Band edge positions of seven metal oxides in contact with aqueous solution at pH 5.6. The lower edge of $E_c$ (blue) and upper edge of $E_v$ (red) are presented along with the band gap in eV. The energy scale is drawn with respect to the normal hydrogen electrode (NHE) and the absolute vacuum scale (AVS) as references. The blue-shaded area represents the conduction band ($E_c$), while the red-shaded area represents the valence band ($E_v$). On the right side the redox potentials of several redox couples are presented.

literature.[35-37] The relevant $E_c$ and $E_v$ levels at pH 5.6 are shown in Table S5 and illustrated in Figure 3 with respect to both the normal hydrogen electrode (NHE) and the absolute vacuum scale (AVS). Moreover, potential redox couples of metal oxides are shown on the right side of Figure 3. $E_H$ values of the redox couples were also determined at pH 5.6 except for those of the redox couples of $Fe^{2+}/Fe^{3+}$ ($Fe^{3+} + e^- \rightarrow Fe^{2+}$, $E^0 = 0.77$ V), $Ce^{3+}/Ce^{4+}$ ($Ce^{4+} + e^- \rightarrow Ce^{3+}$, $E^0 = 1.72$ V), $Cu^+/Cu^{2+}$ ($Cu^{2+} + e^- \rightarrow Cu^+$, $E^0 = 0.16$ V), and $Zn^+/Zn^{2+}$ ($Zn^{2+} + e^- \rightarrow Zn^+$, $E^0 = 1.04$ V), which are not pH dependent (see details in the SI). By aligning $E_v$, $E_c$, and $E_H$, one can easily identify whether the ROS generation reactions are thermodynamically favorable. For example, the reducing power of the excited electrons in the conduction band plays a significant role in the

formation of $O_2^{\bullet-}$. Figure 3 shows that the $E_c$ values of $nTiO_2$ and $nCeO_2$ ($-0.28$ and $-1.69$ eV with respect to NHE; unless indicated, $E_c$ and $E_v$ values are shown with respect to NHE) are less than the $E_H$ of $O_2/O_2^{\bullet-}$ ($-0.2$ eV). This indicates that the potential of $nTiO_2$ and $nCeO_2$ to donate electrons to $O_2$ would lead to the formation of $O_2^{\bullet-}$, which agrees with the experimental results as shown in Table 1. Because the calculated $E_c$ value of $nZnO$ ($-0.12$ eV) is greater than the $E_H$ of $O_2/O_2^{\bullet-}$ ($-0.2$ eV), the reducing power of the photoexcited $nZnO$ is not sufficient to reduce $O_2$. However, $nZnO$ unexpectedly generated $O_2^{\bullet-}$, which is probably because $nZnO$ has n-type character. In aqueous solution $nZnO$ may have an upward-bending conduction band owing to the accumulation of positive charge within the space charge region of the Helmholtz layer.[37] Thus, the actual $E_c$ could become lower than the $E_H$ of $O_2/O_2^{\bullet-}$, which allows the electrons to transfer from the conduction band to the electron acceptor ($O_2$), and thus $O_2^{\bullet-}$ was generated ($O_2 + e^- = O_2^{\bullet-}$). As $nAl_2O_3$ and $nSiO_2$ were not photoexcited because their band gaps are greater than the incident photoenergy (3.4 eV), no $O_2^{\bullet-}$ was detected. The reductive power of the $nCuO$ conduction band potential (0.69 eV) was insufficient to reduce oxygen, so the $nCuO$ suspension could not generate $O_2^{\bullet-}$. Owing to the high $E_c$ of $nFe_2O_3$ (0.46 eV), $O_2$ is not supposed to be reduced to $O_2^{\bullet-}$ in $nFe_2O_3$ suspension either, but a considerable amount of $O_2^{\bullet-}$ was observed. This is reasonable because, similar to $nZnO$, $nFe_2O_3$ is an n-type semiconductor whose conduction band could be bent upward when dispersed in water.[37]

The $E_H$ for $^\bullet OH$ generation is approximately 2.2 V at pH 5.6 with respect to NHE (see SI), which is lower than the $E_v$ values of $nTiO_2$, $nZnO$, $nCuO$, and $nFe_2O_3$ (2.92, 3.08, 2.39, and 2.66 eV, as shown in Table S5), which indicates that the holes of these NPs can theoretically oxidize $H_2O$ into $^\bullet OH$. In fact, $^\bullet OH$ was experimentally detected in all of the above NP suspensions except for $nCuO$, probably because the difference between the $E_v$ of $nCuO$ and $E_H$ of $^\bullet OH$ generation is not substantial. Because UV light cannot excite $nAl_2O_3$ and $nSiO_2$, no $^\bullet OH$ was detected in those suspensions. The $E_H$ for $^\bullet OH$ generation is higher than the $E_v$ of $nCeO_2$ (1.6 eV as shown in Table S5), which indicates that $nCeO_2$ cannot generate $^\bullet OH$.

Similarly, the $E_H$ for $^1O_2/O_2$ is 1.88 eV with respect to NHE at pH 5.6 (see SI), which is lower than the $E_v$ of all of the metal-oxide NPs except $nCeO_2$ (1.6 eV). Thus, $^1O_2$ should be produced in all NP suspensions other than $nCeO_2$, which partially agrees with our experimental observations in Figures 2c. $^1O_2$ was not detected in $nCuO$ and $nFe_2O_3$ suspensions because the $Cu^+/Cu^{2+}$ and $Fe^{2+}/Fe^{3+}$ redox pairs have $E_H$ values significantly less than that of $^1O_2/O_2$, and thus redox reactions with ionic Cu or Fe species could consume the produced $^1O_2$. Interestingly, as mentioned above, $nAl_2O_3$ and

$nSiO_2$ were not supposed to undergo photoexcitation owing to their high $E_g$ value. However, $^1O_2$ was detected in the $nAl_2O_3$ and $nSiO_2$ suspensions, as shown in Figure 2c, which indicates that $nAl_2O_3$ and $nSiO_2$ may operate as a conduit for electrons similar to $nTiO_2$ and promote photochemical reactions without illumination.[20,21]

Figure 3 presents the electronic properties of the bulk scale metal oxides without considering the potential size effect on $E_g$ or the band edge positions.[38] The electronic structures of small NPs (less than 10 nm) are probably different from those of bulk materials. For instance, owing to quantum confinement effects, small NPs likely have larger $E_g$ values than their bulk counterparts, and their band edge positions shift with respect to the positions of bulk materials.[38] However, the NPs used in our study have diameters of 25–50 nm; such NPs have bulk-like electronic structures,[14] and thus changes in electronic structure should not cause differences in the photochemical properties of the tested NPs and their bulk counterparts.

**Antibacterial Activity of NPs and Their Bulk Counterparts toward *E. coli* Cells.** To determine the antibacterial activity of metal-oxide NPs and their bulk counterparts under UV irradiation, we performed a bacterial inhibition assay with *E. coli* cells. Figure 4 shows that in the control test without exposure to metal-oxide particles, the *E. coli* survival rate was not significantly compromised by the 2 h UV irradiation. Moreover, the antibacterial activity under room light conditions was also investigated (see Figure S4). The survival rates ($\log(N_t/N_0)$) of *E. coli* cells were all less than $-0.2$, which indicates that the cellular inhibition from exposure to NPs under room light should be minimal. With addition of particles to the system, the survival rates of *E. coli* cells decreased significantly in the order $nCuO > nTiO_2 > nZnO > nAl_2O_3 > nSiO_2 > nFe_2O_3 > nCeO_2$ for NPs and $bTiO_2 > bZnO > bCuO > bSiO_2 > bCeO_2 > bFe_2O_3$ for the bulk materials. A previous study investigated the antibacterial activity of NPs toward *E. coli* in the presence of sunlight and found an antibacterial ranking of $nZnO > nTiO_2 > nSiO_2$,[8] whereas another study conducted in the absence of sunlight found a ranking of $nZnO > nSiO_2 > nTiO_2$.[28] The differences from our results may be attributed to the sources of or synthetic methods for NPs, experimental conditions (*e.g.*, presence or absence of light illumination, particle size, and NP dose), and solution chemistry (*e.g.*, pH and ionic strength), which largely hamper comparisons among different studies on antibacterial activity for the same NPs. Some antibacterial studies using *E. coli* have demonstrated that $nCuO$ is more toxic than $nZnO$,[10,39] which is consistent with our results.

The antibacterial activity of $nCeO_2$ toward microbial cells has been controversial.[23,25,40] Particularly, whether $nCeO_2$ can induce oxidative stress and inflammation remains debatable.[41−43] As we observed,
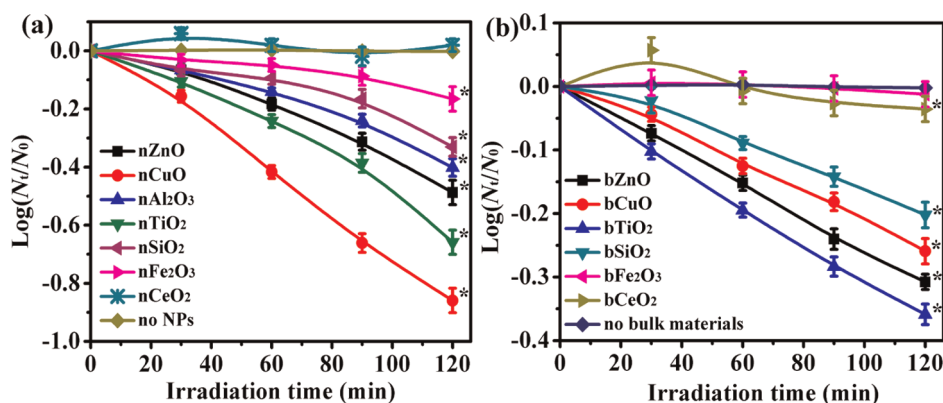
**Figure 4.** Kinetics of *E. coli* inactivation by seven types of metal-oxide NPs (a) and their bulk counterparts (b) under UV irradiation (other conditions were the same as in Figure 1). Asterisks (*) denote a significant difference from the control at the 95% confidence level.

during a short UV exposure time (30 min), $nCeO_2$ may act as a protective layer that shields the *E. coli* cells or absorbs UV irradiation and scavenges the produced ROS.[13] Even the trace amounts of $Ce^{3+}/Ce^{4+}$ ions released may be used as nutrients that eventually boost the growth of *E. coli* cells, as observed in Figure 4. However, after a long UV exposure time (2 h), $nCeO_2$ inhibited the growth of *E. coli* cells, probably owing to the accumulated ROS or other physical damage from $nCeO_2$ attachment.[23]

From the toxicological perspective, particle size significantly changes the antibacterial activity of particles.[1,3,44] One study found no significant size effects on the antibacterial activity of $nTiO_2$, $nSiO_2$, and $nZnO$ toward *E. coli* cells,[8] but most studies have shown that the antibacterial ability increases with decreasing particle size.[1,28,45,46] A comparison between parts a and b in Figure 4 indicates that NPs show higher antibacterial activity to *E. coli* than their bulk counterparts under UV irradiation. For instance, $bFe_2O_3$ exhibited no obvious bactericidal effect, whereas $nFe_2O_3$ inhibited the growth of *E. coli* cells, which was largely due to the enhanced ROS generation of NPs.

**Relationship between the Antibacterial Potency of NPs and ROS Generation.** Oxidative stress from generated ROS is the governing mechanism for the antibacterial activity of engineered NPs, especially under UV illumination,[1,2,5] although nonoxidant paradigms, such as sorption-induced membrane disruption and the release of toxic ions, could also cause cell inhibition or injury.[23,47,48] Establishing a quantitative correlation between the ROS generation and bactericidal effect of NPs would be useful for evaluating and predicting the antibacterial potency of nanomaterials. In line with this effort, we summed the average concentration of each type of ROS for different NPs (see Table 1) and plotted these totals against the survival rates (2 h $\log(N_t/N_0)$) of *E. coli* cells, as shown in Figure 5. Apparently, the bacterial survival rate monotonically decreases with the increasing average concentration of total ROS. According to the Chick−Watson
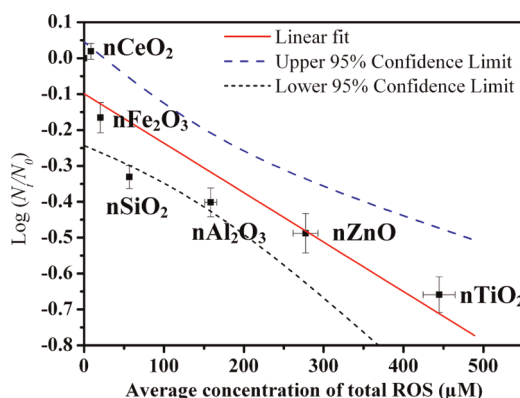


**Figure 5.** Linear regression between the 2 h $\log(N_t/N_0)$ values and the average concentration of total ROS by metal-oxide NPs (Table 1) with the 95% confidence limits shown to indicate the uncertainty in this curve fit. For this linear regression, $R^2$ is 0.84, indicating that the fit equation could explain at least 84% of the variance in the experimental data. Error bars not visible are small or hidden behind the data symbols. Because the bulk materials generally produced insignificant amounts of ROS, we examined the correlation for NPs only.

model (a disinfection kinetic model for *E. coli* inactivation),[7] $\log(N_t/N_0)$ is in a linear relationship with the concentration of disinfectant. Thus, we performed the linear regression for the experimental data in Figure 5 using the linear fit equation:

$$Y = A + B \times X \quad (3)$$

where $Y$ and $X$ are $\log(N_t/N_0)$ and the average concentrations of total ROS. The fit parameters $A$ and $B$ are determined to be $-0.09918$ and $-0.00138$, which are within the intervals of $[-0.24332, 0.04495]$ and $[-0.00207, -0.00068]$ with a confidence level of 95%. According to the *t*-test, the *p* value for parameter $A$ is 0.13715 (not less than the significance level, 0.05), which indicates that $A$ is not statistically different from 0. This is probably reasonable because $A$ represents the background value of $\log(N_t/N_0)$ for *E. coli* cells in the presence of NPs without ROS generation, and thus $A$

should be equal to or less than zero. By contrast, the $p$ value for parameter $B$ is 0.00373 (less than 0.05), which indicates that $B$ is statistically different from 0. The ANOVA gives a $p$ value of 0.00373 (less than 0.05), which indicates that the linear relationship between $\log(N_t/N_0)$ and the average concentration of total ROS is statistically significant.

In addition to ROS generation, we understand some other factors such as ion release may potentially affect the antibacterial activity of NPs. For instance, the antibacterial activity of nZnO may be contributed by both the oxidative stress and the released toxic $Zn^{2+}$.[8,11,13,49] To determine the ion release effect on the antibacterial activity, we monitored the ion release from the suspensions of different metal-oxide NPs under 2 h UV irradiation and only nZnO and nCuO released ions. In nZnO suspension (the total initial concentration of Zn was 5 mg/L), the equilibrium concentration of the released $Zn^{2+}$ was 178.3 $\mu$g/L, as shown in Figure S5a. The antibacterial effect of $Zn^{2+}$ was further analyzed by performing the antibacterial assay with various concentrations of $ZnSO_4$. No significant inhibition toward *E. coli* cells was observed even when $Zn^{2+}$ was 1 mg/L (data not shown), which indicated that the released $Zn^{2+}$ had a minor antibacterial effect. Similarly, as shown in Figure S5b, the released $Cu^{2+}$ was 30.5 $\mu$g/L under 2 h UV irradiation. Both CuO NPs and $Cu^{2+}$ have been demonstrated to be bactericidal,[9,13,50] which explains why nCuO exhibited a strong inhibition toward *E. coli* cells (Figure 4), even without ROS production.

## CONCLUSIONS

To better understand ROS generation mechanisms of metal-oxide NPs and their bulk counterparts, we evaluated the generation kinetics of three types of ROS by seven metal oxides in aqueous solution under UV (365 nm) irradiation. Qualitatively, (1) $nTiO_2$, $nCeO_2$, $nZnO$, $nFe_2O_3$, and bZnO favored $O_2^{\bullet-}$ generation; (2) $nTiO_2$, $nZnO$, $nFe_2O_3$, $bTiO_2$, and bZnO enabled $^{\bullet}OH$ generation; and (3) $nTiO_2$, $nZnO$, $nAl_2O_3$, and $nSiO_2$ produced $^1O_2$. $nTiO_2$ and $nZnO$ generated three types of ROS, whereas other metal oxides produced only one or two types or did not produce any type of ROS. The average concentration of total ROS produced within a specified irradiation period (48 h) followed the order $nTiO_2 > nZnO > nAl_2O_3 > nSiO_2 > nFe_2O_3 > nCeO_2 > nCuO$ for NPs and bZnO > bTiO_2 for bulk materials. By comparing the ROS generation redox potentials with the energy band structures of the metal oxides, with a few exceptions, we could interpret the ROS generation mechanisms of the different metal oxides. This supported the hypothesis that the band edge structures of metal oxides play a crucial role in ROS production in aqueous suspensions. Such a theoretical framework can help to predict ROS production, which may prevent random or exhaustive use of new nanomaterials.

Furthermore, the average concentration of total ROS generated by metal-oxide NPs was correlated with their antibacterial activity ($R^2 = 0.84$). The correlation successfully linked the physicochemical properties and antibacterial activity of NPs, which should provide guidance for the manufacturing of safe and environmentally benign nanomaterials. Even more important, our work also shed light on the applications potential of metal-oxide NPs as antibacterial agents. The current study employed simple experimental approaches (*e.g.*, *E. coli* cells as the sole model bacterium) to facilitate comparisons of the antibacterial activities of different metal-oxide NPs with a reasonable presumption that oxidative stress was the dominant antibacterial mechanism. Thus, it is desirable to holistically take into account other possible antibacterial mechanisms (*e.g.*, released toxic metal ions, adsorption, and material properties) in future studies.

## MATERIALS AND METHODS

**Characterization of NPs and Their Bulk Counterparts.** All metal-oxide NPs and their bulk counterparts were purchased from Sigma-Aldrich, except $nTiO_2$ was purchased from Degussa, $nAl_2O_3$ from Nanostructured & Amorphous Materials, and $bSiO_2$ from Polysciences. The hydrodynamic size and zeta potential of these particles in aqueous suspensions were characterized by dynamic light scattering (DLS) on a Zetasizer Nano ZS instrument (Malvern Instruments, UK). In addition, particles were visualized using a Philips EM420 transmission electron microscope (TEM). The microscope was operated in bright field mode at an acceleration voltage of 28−47 kV. Table S2 summarizes the details of the particle properties, and Figure S1 shows TEM images of various NPs.

**Photochemical Experiments.** For all photochemical experiments, including measurement of ROS production, assessment of antibacterial activity, and measurement of ion release, samples were irradiated with a 4 W compact ultraviolet lamp (UVP model UVGL-21) with a wavelength of 365 nm. The light intensity in the center of the aqueous suspension was approximately 0.78 mW/cm$^2$, as measured by a UVX radiometer (model UVX-25, UVP Co.). In each experiment, 100 mL of aqueous suspension containing 5 mg/L NPs or their bulk counterparts was prepared by diluting the concentrated stock suspension in deionized (DI) water (resistance >18.2 MΩ, Thermo Scientific, USA) in a beaker. The reaction temperature was kept at 22 ± 2 °C by a constant-temperature water bath. Figure S2 provides a schematic of the photochemical experiments, and more experimental details are given in the SI.

**Detection of $O_2^{\bullet-}$, $^{\bullet}OH$, and $^1O_2$.** For $O_2^{\bullet-}$, 100 $\mu$M XTT (2,3-bis(2-methoxy-4-nitro-5-sulfophehyl)-2$H$-tetrazolium-5-carboxanilide) was used as the indicator.[5,51] The XTT stock solution (5.25 mM, Sigma-Aldrich) was stored for no longer than one week at 4 °C. After UV illumination for different periods of time, 1 mL of the suspension was sampled and injected into a quartz vial. The concentration of the orange-colored XTT-formazan (the product resulting from the reduction of XTT by $O_2^{\bullet-}$) was measured using a UV−vis spectrophotometer (Beckman, DU7700) at 470 nm. Exposure tests were run for different time periods up to 48 h until indicator degradation equilibrium was reached.

*p*-Chlorobenzoic acid (20 $\mu$M, Sigma-Aldrich) and furfuryl alcohol (0.85 mM, Sigma-Aldrich) were used as indicators for $^{\bullet}$OH and $^1O_2$, respectively.[5,51] At different UV exposure times, 3 mL of the suspension was collected and filtered by an Amicon Ultra-4 centrifugal ultrafilter with a nominal pore size of 1–2 nm (Amicon Ultracel 3K, Millipore, USA) to remove particles from suspension.[48] The filtration was facilitated by centrifugation (5430R, Eppendorf, Germany) at 7000*g* for 30 min. The background metal ion sorption on the ultrafilter was negligible, as verified previously.[52] The concentrations of *p*CBA and FFA in the collected filtrate were analyzed with a high-performance liquid chromatograph (HPLC, Agilent 1100, USA) equipped with an Agilent Zorbax RX-C 18 column and a diode-array UV detector (237 nm for *p*CBA and 230 nm for FFA). Inductively coupled plasma-mass spectrometry (ICP-MS, Elan DRC II, PerkinElmer, USA) and DLS were used to verify that no undissolved particles were present in the filtrate. *p*CBA was eluted using a mixture of methanol (HPLC grade, Sigma-Aldrich) and DI water at 55:45 (v/v). FFA was eluted using a mixture of 15% methanol and 85% DI water acidified with 0.1% orthophosphoric acid (HPLC grade, Sigma-Aldrich).

The experiments were also carried out in the dark to determine the background ROS production without UV irradiation, which was subtracted from the production under UV irradiation. Control experiments without particles were also performed both with and without UV exposure. Three types of ROS stoichiometricaly react with their corresponding indicators in a mole ratio of 1:1,[5,7,53] and degradation of ROS induced by other side reactions is negligible. The average molar concentration of each type of ROS was computed from the corresponding indicator curve by

$$C = \frac{\int_0^T (C_0 - C_t)\mathrm{d}t}{T} \tag{4}$$

where $C$ is the average molar concentration ($\mu$M) of each type of ROS, $C_0$ is the initial molar concentration of the indicator ($\mu$M), $C_t$ is the molar concentration of the indicator ($\mu$M) after a UV irradiation time of $t$ (h), and $T$ is the exposure time of 48 h.

**Assessment of Antibacterial Activity.** *E. coli* K-12 (strain D21) purchased from the Genetic Stock Center (Department of Biology, Yale University, New Haven, CT, USA) was used to assess the antibacterial activity of various NPs and their counterparts. *E. coli* cells were cultured and harvested according to the method as described previously.[54,55] For the bacterial inhibition assay, 5.0 mg/L particles were homogeneously dispersed in 100 mL of phosphate buffer solution (2 mM phosphate, pH = 7.2) with *E. coli* cells added at a cell density of approximately $10^7$ colony-forming units (cfu)/mL, as indicated by the 660 nm optical density measurement with the same UV–vis spectrophotometer.[54,55] The mixed suspension was exposed to UV light for 2 h, which was chosen because *E. coli* inactivation by UV irradiation alone was not significant within 2 h (results shown below). Moreover, 2 h exposure corresponded to a UV dose of approximately 5616 mW·s/cm$^2$, which was greater than the EPA-proposed minimum UV dosage (12–186 mW·s/cm$^2$) in drinking water disinfection.[56] At different exposure times, the suspension was collected and diluted 100-fold prior to plating 50 $\mu$L onto agar plates (Sautons' liquid medium with 1.5% agar). The total number of viable bacterial colonies was counted after incubation at 37 °C overnight. The results were presented as the percentage of surviving bacteria, which was calculated by dividing the number of colonies on the sample plate ($N_t$) by the number of colonies on a control plate ($N_0$) (no particle exposure) incubated under the same conditions.

**Measurement of Ion Release.** In parallel with the ROS generation and antibacterial assays, metal ion release from the particle suspensions during UV irradiation was investigated using ICP-MS. Briefly, 4 mL of the particle suspension after different UV exposure times was collected and filtered with the same Amicon centrifugal filter. Control experiments were performed in the dark to detect the background metal ion release from particles without UV irradiation; this background concentration was subtracted from the concentrations of released ions under UV irradiation. Section S4 provides detailed acid digestion methods for metal oxides.

**Statistical Analysis.** All photochemical experiments were conducted at least three times to confirm their reproducibility. The data points were expressed as mean values with standard deviations (SD). Statistical significance was evaluated by Student's *t*-test with $p = 0.05$. *t*-Test and analysis of variance (ANOVA) were both performed by Origin 6.1 to evaluate the significance of the regression and confidence levels of the fitting parameters.

*Conflict of Interest:* The authors declare no competing financial interest.

*Supporting Information Available:* A tabulated summary of ROS generation in aqueous suspension containing different engineered NPs, characterization of the metal-oxide particles, photochemical experimental setup, digestion method for ICP-MS analysis, band edge energy of the seven selected metal oxides, redox potentials of the aqueous redox couples, and ion release of ZnO and CuO particles during UV irradiation are available free of charge *via* the Internet at http://pubs.acs.org.

## REFERENCES AND NOTES

1. Nel, A.; Xia, T.; M dler, L.; Li, N. Toxic Potential of Materials at the Nanolevel. *Science* **2006**, *311*, 622–627.
2. Xia, T.; Kovochich, M.; Brant, J.; Hotze, M.; Sempf, J.; Oberley, T.; Sioutas, C.; Yeh, J. I.; Wiesner, M. R.; Nel, A. E. Comparison of the Abilities of Ambient and Manufactured Nanoparticles to Induce Cellular Toxicity According to An Oxidative Stress Paradigm. *Nano Lett.* **2006**, *6*, 1794–1807.
3. Colvin, V. L. The Potential Environmental Impact of Engineered Nanomaterials. *Nat. Biotechnol.* **2003**, *21*, 1166–1170.
4. Ireland, J. C.; Klostermann, P.; Rice, E.; Clark, R. Inactivation of *Escherichia coli* by Titanium Dioxide Photocatalytic Oxidation. *Appl. Environ. Microbiol.* **1993**, *59*, 1668–1670.
5. Brunet, L.; Lyon, D. Y.; Hotze, E. M.; Alvarez, P. J. J.; Wiesner, M. R. Comparative Photoactivity and Antibacterial Properties of C$_{60}$ Fullerenes and Titanium Dioxide Nanoparticles. *Environ. Sci. Technol.* **2009**, *43*, 4355–4360.
6. Wei, C.; Lin, W. Y.; Zainal, Z.; Williams, N. E.; Zhu, K.; Kruzic, A. P.; Smith, R. L.; Rajeshwar, K. Bactericidal Activity of TiO$_2$ Photocatalyst in Aqueous Media: Toward a Solar-Assisted Water Disinfection System. *Environ. Sci. Technol.* **1994**, *28*, 934–938.
7. Cho, M.; Chung, H.; Choi, W.; Yoon, J. Linear Correlation between Inactivation of *E. coli* and OH Radical Concentration in TiO$_2$ Photocatalytic Disinfection. *Water Res.* **2004**, *38*, 1069–1077.
8. Adams, L. K.; Lyon, D. Y.; Alvarez, P. J. Comparative Eco-Toxicity of Nanoscale TiO$_2$, SiO$_2$, and ZnO Water Suspensions. *Water Res.* **2006**, *40*, 3527–3532.
9. Heinlaan, M.; Ivask, A.; Blinova, I.; Dubourguier, H. C.; Kahru, A. Toxicity of Nanosized and Bulk ZnO, CuO and TiO$_2$ to Bacteria *Vibrio fischeri* and Crustaceans *Daphnia magna* and *Thamnocephalus platyurus*. *Chemosphere* **2008**, *71*, 1308–1316.
10. Baek, Y. W.; An, Y. J. Microbial Toxicity of Metal Oxide Nanoparticles (CuO, NiO, ZnO, and Sb$_2$O$_3$) to *Escherichia Coli*, *Bacillus Subtilis*, and *Streptococcus Aureus*. *Sci. Total Environ.* **2011**, *409*, 1603–1608.
11. Emami-Karvani, Z.; Chehrazi, P. Antibacterial Activity of ZnO Nanoparticle on Gram-Positive and Gram-Negative Bacteria. *Afr. J.Microbiol. Res.* **2011**, *5*, 1368–1373.
12. Stoimenov, P. K.; Klinger, R. L.; Marchin, G. L.; Klabunde, K. J. Metal Oxide Nanoparticles As Bactericidal Agents. *Langmuir* **2002**, *18*, 6679–6686.

13. Xia, T.; Kovochich, M.; Liong, M.; Ma dler, L.; Gilbert, B.; Shi, H.; Yeh, J. I.; Zink, J. I.; Nel, A. E. Comparison of the Mechanism of Toxicity of Zinc Oxide and Cerium Oxide Nanoparticles based on Dissolution and Oxidative Stress Properties. *ACS Nano* **2008**, *2*, 2121–2134.

14. Burello, E.; Worth, A. P. A Theoretical Framework for Predicting the Oxidative Stress Potential of Oxide Nanoparticles. *Nanotoxicology* **2011**, *5*, 228–235.

15. Lin, H. F.; Liao, S. C.; Hung, S. W. The DC Thermal Pasma Synthesis of ZnO Nanoparticles for Visible-Light Photocatalyst. *J. Photochem. Photobiol. A: Chem.* **2005**, *174*, 82–87.

16. Du, J.; Gebicki, J. M. Proteins are Major Initial Cell Targets of Hydroxyl Free Radicals. *Int. J.Biochem. Cell Biol.* **2004**, *36*, 2334–2343.

17. Wang, S.; Gao, R.; Zhou, F.; Selke, M. Nanomaterials and Singlet Oxygen Photosensitizers: Potential Applications in Photodynamic Therapy. *J. Mater. Chem.* **2004**, *14*, 487–493.

18. Bakalova, R.; Ohba, H.; Zhelev, Z.; Ishikawa, M.; Baba, Y. Quantum Dots As Photosensitizers? *Nature* **2004**, *22*, 1360–1361.

19. Irwin, F. Biological Effects of the Superoxide Radical. *Arch. Biochem. Biophys.* **1986**, *247*, 1–11.

20. Thomas, C.; Saleh, N.; Tilton, R. D.; Lowry, G. V.; Veronesi, B. Titanium Dioxide (P25) Produces Reactive Oxygen Species in Immortalized Brain Microglia (BV2): Implications for Nanoparticle Neurotoxicity. *Environ. Sci. Technol.* **2006**, *40*, 4346–4352.

21. Long, T. C.; Tajuba, J.; Sama, P.; Saleh, N.; Swartz, C.; Parker, J.; Hester, S.; Lowry, G. V.; Veronesi, B. Nanosize Titanium Dioxide Stimulates Reactive Oxygen Species in Brain Microglia and Damages Neurons *in Vitro*. *Environ. Health Perspect.* **2007**, *115*, 1631–1637.

22. Schubert, D.; Dargusch, R.; Raitano, J.; Chan, S. W. Cerium and Yttrium Oxide Nanoparticles are Neuroprotective. *Biochem. Biophys. Res. Commun.* **2006**, *342*, 86–91.

23. Thill, A.; Zeyons, O.; Spalla, O.; Chauvat, F.; Rose, J.; Auffan, M.; Flank, A. M. Cytotoxicity of CeO₂ Nanoparticles for *Escherichia coli*. Physico-Chemical Insight of the Cytotoxicity Mechanism. *Environ. Sci. Technol.* **2006**, *40*, 6151–6156.

24. Sawai, J.; Kawada, E.; Kanou, F.; Igarashi, H.; Hashimoto, A.; Kokugan, T.; Shimizu, M. Detection of Active Oxygen Generated from Ceramic Powders Having Antibacterial Activity. *J. Chem. Eng. Jpn.* **1996**, *29*, 627–633.

25. Zeyons, O.; Thill, A.; Chauvat, F.; Menguy, N.; Cassier-Chauvat, C.; Oréar, C.; Daraspe, J.; Auffan, M.; Rose, J.; Spalla, O. Direct and Indirect CeO₂ Nanoparticles Toxicity for *Escherichia coli* and *Synechocystis*. *Nanotoxicology* **2009**, *3*, 284–295.

26. Veranth, J. M.; Kaser, E. G.; Veranth, M. M.; Koch, M.; Yost, G. S. Cytokine Responses of Human Lung Cells (BEAS-2B) Treated with Micron-Sized and Nanoparticles of Metal Oxides Compared to Soil Dusts. *Part. Fibre Toxicol.* **2007**, *4*, 1–18.

27. Karlsson, H. L.; Cronholm, P.; Gustafsson, J.; Möller, L. Copper Oxide Nanoparticles are Highly Toxic: A Comparison between Metal Oxide Nanoparticles and Carbon Nanotubes. *Chem. Res. Toxicol.* **2008**, *21*, 1726–1732.

28. Jiang, W.; Mashayekhi, H.; Xing, B. Bacterial Toxicity Comparison between Nano- and Micro-Scaled Oxide Particles. *Environ. Pollut.* **2009**, *157*, 1619–1625.

29. Choi, O.; Hu, Z. Size Dependent and Reactive Oxygen Species Related Nanosilver Toxicity to Nitrifying Bacteria. *Environ. Sci. Technol.* **2008**, *42*, 4583–4588.

30. Auffan, M.; Rose, J.; Wiesner, M. R.; Bottero, J. Y. Chemical Stability of Metallic Nanoparticles: A Parameter Controlling their Potential Cellular Toxicity *in Vitro*. *Environ. Pollut.* **2009**, *157*, 1127–1133.

31. Grätzel, M. Photoelectrochemical Cells. *Nature* **2001**, *414*, 338–344.

32. Vecitis, C. D.; Zodrow, K. R.; Kang, S.; Elimelech, M. Electronic-Structure-Dependent Bacterial Cytotoxicity of Single-Walled Carbon Nanotubes. *ACS Nano* **2010**, *4*, 5471–5479.

33. Mëïiamlin, V. A.; Pleskov, I. V. *Electrochemistry of Semiconductors*; Plenum Press: New York, 1967.

34. Butler, M. A.; Ginley, D. S. Prediction of Flatband Potentials at Semiconductor-Electrolyte Interfaces from Atomic Electronegativities. *J. Electrochem. Soc.* **1978**, *125*, 228–232.

35. Zhang, Y.; Chen, Y.; Westerhoff, P.; Hristovski, K.; Crittenden, J. C. Stability of Commercial Metal Oxide Nanoparticles in Water. *Water Res.* **2008**, *42*, 2204–2212.

36. Li, K.; Zhang, W.; Huang, Y.; Chen, Y. Aggregation Kinetics of CeO₂ Nanoparticles in KCl and CaCl₂ Solutions: Measurements and Modeling. *J. Nanopart. Res.* **2011**, *13*, 6483–6491.

37. Xu, Y.; Schoonen, M. A. A. The Absolute Energy Positions of Conduction and Valence Bands of Selected Semiconducting Minerals. *Am. Mineral.* **2000**, *85*, 543–556.

38. Satoh, N.; Nakashima, T.; Kamikura, K.; Yamamoto, K. Quantum Size Effect in TiO₂ Nanoparticles Prepared by Finely Controlled Metal Assembly on Dendrimer Templates. *Nat. Nanotechnol.* **2008**, *3*, 106–111.

39. Ren, G.; Hu, D.; Cheng, E. W. C.; Vargas-Reus, M. A.; Reip, P.; Allaker, R. P. Characterisation of Copper Oxide Nanoparticles for Antimicrobial Applications. *Int. J. Antimicrob. Agents* **2009**, *33*, 587–590.

40. Pelletier, D. A.; Suresh, A. K.; Holton, G. A.; McKeown, C. K.; Wang, W.; Gu, B.; Mortensen, N. P.; Allison, D. P.; Joy, D. C.; Allison, M. R.; Brown, S. D.; Phelps, T. J.; Doktycz, M. J. Effects of Engineered Cerium Oxide Nanoparticles on Bacterial Growth and Viability. *Appl. Environ. Microbiol.* **2010**, *76*, 7981–7989.

41. Horie, M.; Nishio, K.; Kato, H.; Fujita, K.; Endoh, S.; Nakamura, A.; Miyauchi, A.; Kinugasa, S.; Yamamoto, K.; Niki, E. Cellular Responses Induced by Cerium Oxide Nanoparticles: Induction of Intracellular Calcium Level and Oxidative Stress on Culture Cells. *J. Biochem.* **2011**, *150*, 461–471.

42. Park, E. J.; Choi, J.; Park, Y. K.; Park, K. Oxidative Stress Induced by Cerium Oxide Nanoparticles in Cultured BEAS-2B Cells. *Toxicology* **2008**, *245*, 90–100.

43. Lin, W.; Huang, Y.; Zhou, X. D.; Ma, Y. Toxicity of Cerium Oxide Nanoparticles in Human Lung Cancer Cells. *Int. J. Toxicol.* **2006**, *25*, 451–457.

44. Lewinski, N.; Colvin, V.; Drezek, R. Cytotoxicity of Nanoparticles. *Small* **2008**, *4*, 26–49.

45. Simon-Deckers, A. l.; Loo, S.; Mayne-L'hermite, M.; Herlin-Boime, N.; Menguy, N.; Reynaud, C. c.; Gouget, B.; Carriére, M. Size-, Composition- and Shape-Dependent Toxicological Impact of Metal Oxide Nanoparticles and Carbon Nanotubes toward Bacteria. *Environ. Sci. Technol.* **2009**, *43*, 8423–8429.

46. Osamu, Y. Influence of Particle Size on the Antibacterial Activity of Zinc Oxide. *Int. J. Inorg. Mater.* **2001**, *3*, 643–646.

47. Zhang, W.; Kalive, M.; Capco, D. G.; Chen, Y. Adsorption of Hematite Nanoparticles onto Caco-2 Cells and the Cellular Impairments: Effect of Particle Size. *Nanotechnology* **2010**, *21*, 1–9.

48. Zhang, W.; Yao, Y.; Sullivan, N.; Chen, Y. Modeling the Primary Size Effects of Citrate-Coated Silver Nanoparticles on Their Ion Release Kinetics. *Environ. Sci. Technol.* **2011**, *45*, 4422–4428.

49. Ivask, A.; Bondarenko, O.; Jepihhina, N.; Kahru, A. Profiling of the Reactive Oxygen Species-Related Ecotoxicity of CuO, ZnO, TiO₂, Silver and Fullerene Nanoparticles Using a Set of Recombinant Luminescent *Escherichia coli* Strains: Differentiating the Impact of Particles and Solubilised Metals. *Anal. Bioanal. Chem.* **2010**, *398*, 1–16.

50. Gunawan, C.; Teoh, W. Y.; Marquis, C. P.; Amal, R. Cytotoxic Origin of Copper(II) Oxide Nanoparticles: Comparative Studies with Micron-Sized Particles, Leachate, and Metal Salts. *ACS Nano* **2011**, *5*, 7214–7225.

51. Lee, J.; Fortner, J. D.; Hughes, J. B.; Kim, J. H. Photochemical Production of Reactive Oxygen Species by C₆₀ in the Aqueous Phase During UV Irradiation. *Environ. Sci. Technol.* **2007**, *41*, 2529–2535.

52. Li, Y.; Zhang, W.; Li, K. G.; Yao, Y.; Niu, J. F.; Chen, Y. S. Oxidative Dissolution of Polymer-Coated CdSe/ZnS Quantum Dots under UV Irradiation: Mechanisms and Kinetics. *Environ. Pollut.* **2012**, *164*, 259–266.

53. Llansola Portolés, M. J.; David Gara, P. M.; Kotler, M. n. L.; Bertolotti, S.; San Román, E.; Rodríguez, H. n. B.; Gonzalez, M. n. C. Silicon Nanoparticle Photophysics and Singlet Oxygen Generation. *Langmuir* **2010**, *26*, 10953–10960.

54. Zhang, W.; Rittmann, B.; Chen, Y. Size Effects on Adsorption of Hematite Nanoparticles on *E. coli* Cells. *Environ. Sci. Technol.* **2011**, *45*, 2172–2178.

55. Zhang, W.; Yao, Y.; Chen, Y. S. Imaging and Quantifying the Morphology and Nanoelectrical Properties of Quantum Dot Nanoparticles Interacting with DNA. *J. Phys. Chem. C* **2011**, *115*, 599–606.

56. Clarke, S.; Bettin, W. Ultraviolet Light Disinfection in the Use of Individual Water Purification Devices. U.S. Army Center for Health Promotion and Preventive Medicine: Massachusetts, APG, 2006.